The equatorial shape and gravity field of Mercury from MESSENGER flybys 1 and 2

David E. Smith [a], Maria T. Zuber [a,*], Roger J. Phillips [b], Sean C. Solomon [c], Gregory A. Neumann [d], Frank G. Lemoine [d], Stanton J. Peale [e], Jean-Luc Margot [f], Mark H. Torrence [g], Matthieu J. Talpe [a], James W. Head III [h], Steven A. Hauck II [i], Catherine L. Johnson [j], Mark E. Perry [k], Olivier S. Barnouin [k], Ralph L. McNutt Jr. [k], Jürgen Oberst [l]

[a] Department of Earth, Atmospheric and Planetary Sciences, Massachusetts Institute of Technology, Cambridge, MA 02139, USA
[b] Planetary Science Directorate, Southwest Research Institute, Boulder, CO 80302, USA
[c] Department of Terrestrial Magnetism, Carnegie Institution of Washington, Washington, DC 20015, USA
[d] Solar System Exploration Division, NASA Goddard Space Flight Center, Greenbelt, MD 20771, USA
[e] Department of Physics, University of California, Santa Barbara, CA 93106, USA
[f] Department of Earth and Space Sciences, University of California, Los Angeles, CA 90095, USA
[g] Stinger Ghaffarian Technologies, Inc., 7701 Greenbelt Road, Suite 400, Greenbelt, Maryland 20770, USA
[h] Department of Geological Sciences, Brown University, Providence, RI 02912, USA
[i] Department of Geological Sciences, Case Western Reserve University, Cleveland, OH 44106, USA
[j] Department of Earth and Ocean Sciences, University of British Columbia, Vancouver, BC, Canada V6T 1Z4
[k] Space Department, Johns Hopkins University Applied Physics Laboratory, Laurel, MD 20723-6099, USA
[l] German Aerospace Center, Institute of Planetary Research, D-12489 Berlin, Germany

ARTICLE INFO

ABSTRACT

On 14 January and 6 October 2008 the MESSENGER spacecraft passed within 200 km of the surface of Mercury. These flybys by MESSENGER provided the first observations of Mercury from a spacecraft since the Mariner 10 flybys in 1974 and 1975. Data from the Mercury Laser Altimeter (MLA) provided new information on the equatorial shape of Mercury, and Doppler tracking of the spacecraft through the flybys provided new data on the planet's gravity field. The MLA passes were on opposite hemispheres of the planet and span collectively ∼40% of the equatorial circumference. The mean elevation of topography observed during flyby 1, in the longitude range 0–90°E, is greater than that seen during flyby 2 in the longitude range 180–270°E, indicating an offset between centers of mass and figure having a magnitude and phase in general agreement with topography determined by Earth-based radar. Both MLA profiles are characterized by slopes of ∼0.015° downward to the east, which is consistent with a long-wavelength equatorial shape defined by a best-fitting ellipse. The Doppler tracking data show sensitivity to the gravitational structure of Mercury. The equatorial ellipticity of the gravitational field, $C_{2,2}$, is well determined and correlates with the equatorial shape. The $S_{2,2}$ coefficient is ∼0, as would be expected if Mercury's coordinate system, defined by its rotational state, is aligned along its principal axes of inertia. The recovered value of the polar flattening of the gravitational potential, J_2, is considerably lower in magnitude than the value obtained from Mariner 10 tracking, a result that is problematic for internal structure models. This parameter is not as well constrained as the equatorial ellipticity because the flyby trajectories were nearly in the planet's equatorial plane. The residuals from the Doppler tracking data suggest the possibility of mascons on Mercury, but flyby observations are of insufficient resolution for confident recovery. For a range of assumptions on degree of compensation and crustal and mantle densities, the allowable crustal thickness is consistent with the upper limit of about 100 km estimated from the inferred depth of faulting beneath a prominent lobate scarp, an assumed ductile flow law for crustal material, and the condition that temperature at the base of the crust does not exceed the solidus temperature. The MESSENGER value of $C_{2,2}$ has allowed an improved estimate of the ratio of the polar moment of inertia of the mantle and crust to the full polar moment (C_m/C), a refinement that strengthens the conclusion that Mercury has at present a fluid outer core.

© 2010 Elsevier Inc. All rights reserved.

* Corresponding author. Fax: +1 617 253 7651.
  E-mail address: zuber@mit.edu (M.T. Zuber).

1. Introduction

The first spacecraft to approach Mercury was Mariner 10. Launched in 1973, the spacecraft successfully completed three fly-bys of the innermost planet in March and September 1974 and March 1975 and provided most of our current knowledge of the planet until early 2008. Mariner 10 was the first spacecraft to use the flyby of a planet (Venus) as a gravity assist to reach its tar-get body (Mercury). For two of the Mariner 10 flybys the spacecraft flew sufficiently close to the planet to enable the mass, gravita-tional polar flattening, and gravitational equatorial ellipticity of Mercury to be estimated. Earth-based radar observations compiled by Anderson et al. (1996) indicated a nearly spherical planet, slightly flattened at the poles, and with a mildly elongated equator. The MErcury Surface, Space ENvironment, GEochemistry, and Ranging (MESSENGER) spacecraft, only the second probe to encounter the innermost planet, flew by Mercury on 14 January and 6 October 2008. At the time of those flybys, the first two of three in all, the values of Mercury's mass and gravity field obtained by Mariner 10 were the *a priori* values used for the trajectory cal-culations that placed the MESSENGER spacecraft within 200 km of the surface at closest approach.

The MESSENGER payload includes the Mercury Laser Altimeter (MLA) (Cavanaugh et al., 2007) and a gravity science investigation that uses the spacecraft tracking system (Srinivasan et al., 2007). During both of the first two flybys the laser altimeter was operated while within range of the planet and the spacecraft was tracked at X-band frequency by the Deep Space Network (DSN), the latter providing high-quality Doppler range-rate observations of the spacecraft motion relative to Earth. During those flybys, the space-craft was within 100,000 km of the planet for ~10 h. The inertial direction of the spacecraft was changed by approximately 20° by each encounter. The ground tracks of both flybys across the surface of the planet were almost equatorial at ~5° south latitude and on opposite sides of the planet. The MLA ranged to the surface of the planet near closest approach on each flyby for ~10 min, and data collected are used in this paper to derive the physical shape of Mer-cury's equatorial region. The Doppler tracking data are used to esti-mate the mass and long-wavelength gravity field of Mercury.

During flyby 1 (M1), MESSENGER was in the shadow of Mercury for ~13 min, which included the point of closest approach, and was eclipsed from Earth for 48 min, emerging from behind the planet a few minutes prior to closest approach. Subsequent to the flyby, the spacecraft velocity vector was approximately aligned with the line-of-sight direction to Earth. During flyby 2 (M2), the spacecraft was in full sunlight throughout the encounter and was observable from Earth for the entire time with a direction of travel approximately perpendicular to the Earth-MESSENGER direction, so the Doppler signal was largely the radial component of velocity with respect to the planet.

The Mercury-MESSENGER range during the closest part of the two encounters is shown as a function of planetary longitude in Fig. 1. The figure illustrates that the spacecraft traversed 75% of the span of longitudes on the planet on the two flybys at altitudes of less than 2 Mercury radii and therefore was perturbed primarily by the longest wavelengths of the Mercury gravity field, i.e., those of degree and order 2. Fig. 1 also shows the coverage obtained by MLA.

During flyby 3, on 29 September 2009, the MESSENGER space-craft unfortunately entered safe mode shortly before closest ap-proach. No altimetry data were collected, and no tracking that could be used to improve the equatorial shape was obtained.

2. Tracking and altimetry data sets

2.1. Altimetry

MLA is a single-beam laser altimeter with a beam divergence of 100 microradians illuminating, when nadir pointed, a 20-m-diam-eter spot from 200-km altitude and a 100-m-diameter spot from 1000 km (Cavanaugh et al., 2007). The laser pulse rate is 8 Hz, so the distance between measurements is about 500 m when the spacecraft orbital velocity is 4 km/s. During the flybys the nominal velocity of the spacecraft across the surface was 5–6 km/s (Solo-mon et al., 2008). The normal operating state of MLA during flyby operations was not nadir oriented because of the requirement that the spacecraft be oriented so that its sunshade protects the instru-ments from direct sunlight (Santo et al., 2001). Consequently, the area illuminated by MLA was generally elliptical in shape, which has the effect of spreading the laser return pulse and decreasing the accuracy of the range measurement depending on the emission angle, ε, the angle between the range vector and the surface normal.

The ranges to the surface and emission angles are shown in Fig. 2 for both flybys, and Fig. 3 shows the altimetry coverage. On both flybys altimetry data were obtained at an initial range of 700–800 km at ε of nearly 70°. This ability to range continuously at such large emission angles is a result of stronger signal return than expected, attributable in part to the structure and roughness of Mercury's surface (Zuber et al., 2008). Towards the end of both tracks MLA became nadir pointed and continued to range to the surface out to distances of nearly 1700 km, greater than the de-signed range of about 1200 km (Sun et al., 2004; Cavanaugh et al., 2007).

The nominal range precision of MLA is approximately ±10 cm on flat surfaces with strong signals (Cavanaugh et al., 2007). How-ever, the range variation and the large emission angles during the flybys degrade the precision by approximately $1/\cos(\varepsilon)$. The accu-racy is dependent on the knowledge of the spacecraft position, par-ticularly in the direction radial to the planet. During the flybys the orbital position with respect to the center of mass of Mercury is be-lieved to be at the tens-of-meters level in the radial direction and
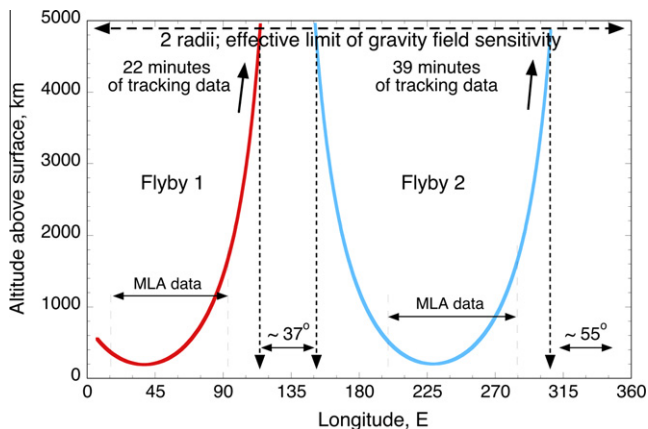

Fig. 1. Altitude of MESSENGER near closest approach on flybys 1 and 2 showing coverage of MLA and the effective altitude limit of gravity field sensitivity of ~2 Mercury radii.
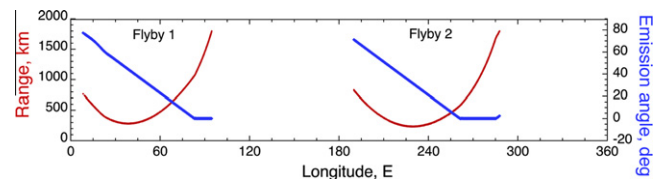

Fig. 2. Range and emission angle for MLA during MESSENGER flybys 1 and 2.
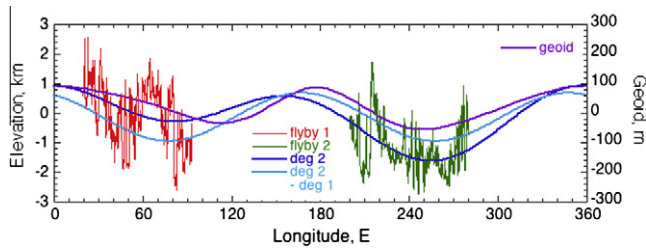
Fig. 3. MLA elevations and coverage for flybys 1 and 2. Elevations are with respect to a sphere of radius 2440 km (Zuber et al., 2008). The two flybys were on opposite sides of the planet and covered a total of about 170° in longitude or 41% of the equatorial circumference. Also shown is a spherical harmonic degree-2 fit to the altimetry (in dark blue) and the fit with the degree-1 terms associated with the COF-COM offset removed (in light blue) for comparison with the geoid, which does not contain these terms. The geoid is shown in purple, but note the different vertical scale from that for the altimetry. The general correspondence between the equatorial shape and the geoid is apparent.

places a probable accuracy limit on the radii derivable from the altimetry data. Unfortunately, the accuracy cannot be rigorously verified, although comparison with radar data suggests a probable accuracy of 16 m (cf. Section 3.3 and Table 1).

2.2. Doppler tracking

The MESSENGER spacecraft was tracked during both flybys by the DSN at X-band frequency, ~8.4 GHz, with a quality of order 0.1 mm/s at a 10-s rate (Srinivasan et al., 2007). For both flybys we analyzed 14-day spans of data centered on the time of closest approach. In both cases the distance of the spacecraft from the planet 7 days before and after closest approach was approximately 3×10^6 km. The total data set consists of ~123,000 Doppler observations.

During flyby 1 the spacecraft was tracked by the DSN throughout the encounter except for a period of approximately 45 min prior to closest approach when MESSENGER was occulted by the planet (as viewed from Earth). The probe emerged from behind the planet approximately 5 min before closest approach, when tracking of the spacecraft resumed.

The residuals to the tracking data during the 12 h centered on closest approach for each flyby, relative to predictions using the gravity model derived previously from Mariner 10 (M10) tracking (Anderson et al., 1987), are shown in Fig. 4. If the M10 field were able to satisfy the MESSENGER tracking data, the residual pattern would be flat except for any unmodeled systematic errors. The amplitudes and pattern of the residuals indicate that improvement in the modeling of the forces on the spacecraft, principally gravity, is required.

3. Equatorial shape

3.1. Mean radius and equatorial axes

A plot of the MLA data versus longitude reveals qualitative information about the equatorial shape of Mercury (Fig. 3). The
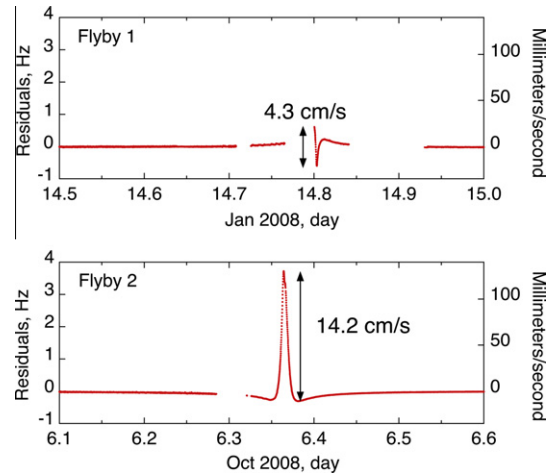

Fig. 4. Doppler tracking residuals relative to the *a priori* gravity model from Mariner 10 (Anderson et al., 1987) for 12 h centered approximately on the points of closest approach for the two flybys. On flyby 1, immediately before closest approach, the spacecraft was occulted from Earth for 47 min. The figures are on the same vertical scale, and it is probable if the spacecraft had not been occulted by the planet that the residual would have been of similar size to that for flyby 2.

mean elevation of the M1 data (first quadrant, 0–90°E) is greater than the mean of the M2 data (third quadrant, 180–270°E), indicating the general direction of the offset of the center of figure (COF) from the center of mass (COM). Both MLA profiles show similar slopes of ~0.015° downward to the east, which combined with the ~180° difference in longitudinal location of the profiles is indicative of the long-wavelength equatorial shape.

3.2. Spherical harmonic expansion of equatorial shape

Quantitatively, the long-wavelength shape of the equator can be obtained from a second-degree spherical harmonic expansion of the M1 and M2 MLA data. Because of the limited latitude range of the data (99.9% lie in the range 0–5°S), a least-squares solution is unstable if latitude-dependent terms are included. By making the approximation that the 13,234 MLA observations were all acquired at the equator, a stable five-term, longitude-only expansion results. The spherical harmonic coefficients estimated are the assumed mean radius perturbation, $c_{0,0}$; the first-degree terms $c_{1,1}$ and $s_{1,1}$, which are directly related to the magnitude, F_1, and orientation, φ_1, of the equatorial projection of the COF-COM offset; and the second-degree terms $c_{2,2}$ and $s_{2,2}$, which are directly related to the magnitude $(a - b)$ and orientation, φ_2, of the elliptical shape of an equator having semi-major and semi-minor axes a and b, respectively, where all double subscripts are respectively harmonic degree and order.

The equatorial elevation curve resulting from the fit to the M1 and M2 data is shown in Fig. 3 for the full set of five spherical harmonic coefficients. A curve is also shown with the degree-1 terms removed for better comparison to the geoid, as these terms do not appear in the gravitational potential for a COM-centered coordi-

Table 1
Equatorial shape parameters. The quantities a and b are axes of the ellipse fit to equatorial topography, φ_2 is the orientation of the a axis, F_1 is the magnitude of the equatorial projection of the COF-COM offset, and φ_1 is the longitudinal direction of this component.

	MLA	Anderson et al. (1996)	Radar, 1978–1997	MLA + radar, $\sigma_{MLA} = 16$ m
$(a - b)/a \times 10^6$	664 ± 29	540 ± 54	612 ± 250	636 ± 139
φ_2, °E	−12.5 ± 1.0	−15.3 ± 2.9	−24.4 ± 5.3	−13.5 ± 1.2
F_1, m	683 ± 146	640 ± 78	614 ± 296	639 ± 170
φ_1, °E	62.2 ± 7.3	40.5 ± 6.9	52.9 ± 17.9	52.4 ± 5.6

nate system. The correlation of the equatorial shape with the geoid is evident.

3.3. Comparison with Earth-based radar topography

It is of interest to compare the equatorial shape of Mercury determined by MLA with observations from Earth-based radar that previously sampled low-latitude regions of Mercury (Anderson et al., 1996). Table 1 presents a comparison of MLA with two different radar solutions.

In the first case (Anderson et al., 1996), results for the radar-derived shape were obtained as part of a Solar System ephemeris solution that contained 73,535 observations (of which 629 were radar ranging observations acquired during the period 1966–1990) and 189 solved parameters (of which nine describe the shape of Mercury).

In the second case, radar shape results were obtained from data that include newer radar observations (1991–1997) provided by J.D. Anderson and that exclude the noisier data acquired before 1978. For this case, the spherical harmonic model coefficients (which included the latitude-dependent Legendre polynomial terms) were obtained by a fit to 378 radar elevations that were the range residuals from an ephemeris program, rather than estimated in a simultaneous solution within the ephemeris program. Employing a standard weighting scheme of inverse uncorrelated variance, a least-squares solution using the 1-σ values reported in the radar data set yields results that are reasonably close to the MLA results. The differences are less than 15%, with the notable exception of the orientation of the equatorial shape ellipse, φ_2 (a 12° difference). The longitudinal sampling of MLA provided by the M1 and M2 geometries and the large number of observations place a strong constraint on φ_2.

We combined the complete radar data set (724 radar ranging points) with the MLA data set and obtained a weighted least-squares solution (Table 1) by treating the error in the MLA data as a single variable parameter, σ_{MLA}. The most important geophysical shape parameter is arguably φ_2 because of the possible correlation of second-degree shape with the corresponding gravitational equatorial ellipticity (defined by the equatorial moments of inertia, A and B). Fig. 5 plots the standard deviation of the fit, σ_{fit}, and φ_2

Fig. 5. Orientation, φ_2, of the a axis of the equatorial shape ellipse estimated from the combined MLA and radar data sets plotted as a function of assumed error, σ_{MLA}, in MLA elevation values. Also plotted is the standard deviation, σ_{fit}, of the weighted fit, with the best fit occurring for $\sigma_{MLA} = 16$ m, for which $\varphi_2 = (-13.5 \pm 1.2)°$E. As σ_{MLA} becomes small, the solution is dominated by MLA data. Because the solution contains latitude-dependent terms, it starts to become unstable, leading to rapid increases in σ_{fit} and the error in the φ_2 estimate. The results for small σ_{MLA} should not be compared to the MLA-only value of φ_2 in Table 1, as the latter was obtained from a latitude-independent model.

against σ_{MLA}, and the best fit occurs at $\sigma_{MLA} = 16$ m, for which $\varphi_2 = -13.5 \pm 1.2°$E. Excluding the radar data before 1978 decreases φ_2 to $-9.3 \pm 1.8°$E.

All radar-only or radar/MLA solutions that we examined have unstable estimates of the z (orthogonal to equatorial plane) component of the COF-COM offset, meaning that different strategies for data inclusion (e.g., radar-only over different acquisition intervals, combined radar and MLA solutions) lead to substantially different results. The only common behavior is that the center of figure is always shifted to the northern hemisphere. The equatorial projection of the COF-COM offset, F_1, is stable under the same circumstances (e.g., Table 1) with a magnitude in the range ~600–700 m.

4. Gravity model development

4.1. Spherical harmonic solutions

The solutions for the orbit and gravity field were conducted in a Mercury-centered coordinate system using the standard expression (Kaula, 1966) for the gravitational potential in terms of normalized spherical harmonic coefficients, $C_{l,m}$ and $S_{l,m}$ of degree l and order m, where the normalization, $N_{l,m}$ (Kaula, 1966) is

$$N_{l,m} = [(l-m)!(2l+1)(2-\delta_{0,m})/(l+m)!]^{1/2}, \qquad (1)$$

and $\delta_{0,m}$ is the Kronecker delta.

The software used for the analysis was the NASA Goddard Space Flight Center GEODYN Program System (Rowlands et al., 1993; McCarthy et al., 1994). We initially processed each flyby separately (Fig. 4), and we subsequently produced a series of joint solutions for the two trajectories, gravity field parameters (spherical harmonic coefficients, surface mass anomalies, or some combination), and a set of parameters that described the area/mass of the spacecraft, position of the phase center of the antenna, and related quantities.

Tracking data covering 6–14 days centered on the flyby were analyzed, including data obtained outward to approximately 3×10^6 km distance from Mercury. To ensure that we included all data sensitive to Mercury's gravity field, we obtained solutions for data sets covering 6, 8, 10, 12, and 14 days.
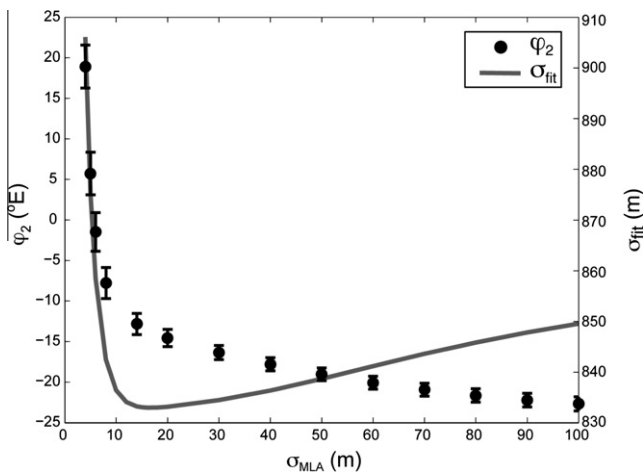
Table 2
Major parameters adjusted, modeled, or estimated in the solutions. The uncertainties are the formal errors based on a data weight of 1 cm/s and need to be adjusted.

Parameter	Modeled/estimated/adjusted	A priori value
GM	Estimated	22032.09 km^3 s^{-2}; M10[a]
Gravity coefficients	Estimated	$J_2 = 6.0 \times 10^{-5}$; $C_{2,2} = 1.0 \times 10^{-5}$; M10[a]
Antenna location	Estimated in some solutions; modeled	SPICE[b] kernels
Spacecraft attitude	Modeled	SPICE kernels
Solar radiation	Estimated	
Position of Mercury	Adjusted in some solutions	DE421[c]
Doppler biases	Estimated in some solutions	None
Spacecraft shape	Modeled	Box and plate
Mercury albedo	Not included	None

Estimated: parameter value obtained in the solution.
Modeled: parameter values assumed/obtained from external source.
Adjusted: a priori value of parameter changed.
  [a] Mariner 10 results (Anderson et al., 1987).
  [b] SPICE = kernels containing information on Spacecraft ephemeris; Planet, satellite, or comet ephemeris; Instrument description; C-matrix (pointing); Events.
  [c] DE = dynamic ephemeris.

The parameters we included in the analysis are shown in Table 2, either as estimated or modeled parameters. For some of these parameters we had good *a priori* values, such as the attitude information, and for others including the gravity field and the position of Mercury, we needed to estimate or change from solution to solution to assess whether they were important or if their values could influence the solution for other parameters.

The primary parameter that we used to assess the quality of the estimated solution for the gravity field was the range of the data residuals from a data reduction run around the time of closest approach. In Fig. 4 these values were 4.3 cm/s and 14.2 cm/s for flybys 1 and 2, respectively, and these figures were used to assess the field derived from Mariner 10 tracking data.

Our initial solutions estimated only the *GM* term in the gravitational potential, where *G* is the universal constant of gravitation and *M* is the mass of Mercury, on the assumption that all other gravity coefficients were zero. Estimates were made for the individual flybys and combined. Subsequent solutions included the $C_{2,0}$ and $C_{2,2}$ terms, all others being set to zero, and also solutions including $S_{2,2}$. Table 3 shows solutions for *GM* and second-degree gravity potential coefficients obtained simultaneously with the flyby trajectories using a data weight of 1 cm/s. The table also shows the results from Mariner 10 (Anderson et al., 1987) converted to their normalized values for comparison. The latter were the *a priori* values for analysis of the MESSENGER data. Unfortunately, the Mariner 10 tracking data have been lost and are therefore no longer available for re-analysis in combination with the MESSENGER tracking data.

The results in Table 3 for *GM* are all less than the Mariner 10 value, but they are within the M10 error bars, and this outcome was consistent throughout the analysis of the MESSENGER flybys and the many solutions we obtained and investigated. The two values for $C_{2,0}$ are both very small, and they are noticeably affected by the inclusion of the $S_{2,2}$ coefficient in the solution. The low value of $C_{2,0}$ presents geophysical difficulties, discussed in Section 5.2. It can be argued, of course, that trying to obtain an estimate of $C_{2,0}$ (representing the gravitational polar flattening) only from near-equatorial tracking data is challenging. However, the solution was a free adjustment, and the formal standard deviation is only 50% larger than that of $C_{2,2}$, which represents the gravitational ellipticity of the equator and which we believe is well determined on the basis of the good equatorial coverage from the two flybys. Fig. 6 shows the comparative sensitivity of *GM* and $C_{2,0}$ in the equatorial plane as a function of distance from the planet for a normalized $C_{2,0} = -0.89 \times 10^{-5}$ (equivalent to $J_2 = 2 \times 10^{-5}$), one of the smaller values of $C_{2,0}$ obtained in our solutions. Fig. 6 indicates that $C_{2,0}$ contributes 10^{-5} of *GM* when close to Mercury, diminishing to zero at distance. This contribution is equal to the change in *GM* that we observe in the MESSENGER solutions from the Mariner 10 results and is separable if sufficient coverage in data is employed. Table 3 shows that *GM* adjusts to the lower value even when $C_{2,0}$ is not adjusted, indicating independence from $C_{2,0}$.
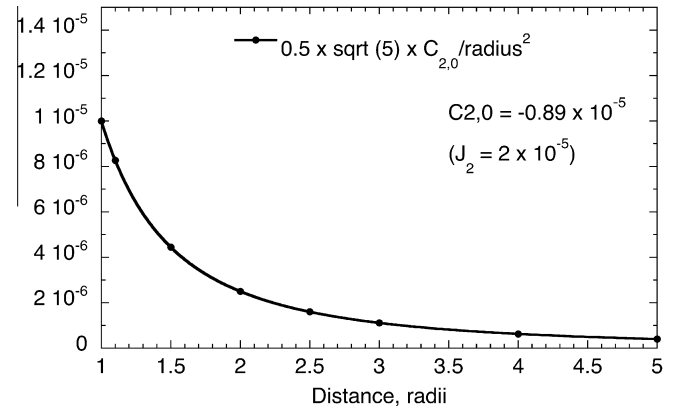

Fig. 6. Ratio of planetary flattening $C_{2,0}$ compared to Mercury's central mass term. Close to the planet the influence of the flattening is $\sim 10^{-5}$. At three Mercury radii the comparative influence is $\sim 10^{-6}$. The data used in the analysis extended to over 1200 radii ($\sim 3 \times 10^6$ km).

The two MESSENGER values of $C_{2,2}$ shown in Table 3 are the same within any reasonable error estimate and are consistent with the Mariner 10 result. The estimate of $S_{2,2}$ was obtained because none of the prior solutions had reduced the spread of Doppler residuals around closest approach to less than 2 or 3 cm/s, suggesting that major sources of gravity signal remained to be identified. For geophysical reasons (see Section 5.1), the value of $S_{2,2}$ is expected to be identically zero, so estimating its value represents a mechanism for making an assessment of the quality of the field.

The right column of Table 3 shows the spread of the Doppler residuals at closest approach. The table suggests that improving the value of *GM*, even with zero values for the other gravity coefficients, makes a substantial improvement in the spread of residuals. Adjusting $S_{2,2}$ does nothing for the residual range but does change *GM* and $C_{2,0}$, making both smaller in amplitude.

The relatively large remaining Doppler residuals around closest approach suggested that we needed to increase the number of gravity parameters and explore other possible causes of the residual pattern. The gravity representations we examined included gravity anomalies near the ground tracks and 3×3 and 4×4 spherical harmonic solutions (i.e., fully expanded to degree and order 3 and 4). In addition, we assessed the influence of an error in the position of Mercury, errors in our solar radiation model for the spacecraft, biases in the Doppler tracking, and the effect of the solar gravity tide expressed through the Love number, k_2. None of these additional effects produced any significant improvement or change in the residual pattern.

We obtained a series of spherical harmonic solutions starting from the combined solution in Table 3 for *GM*, $C_{2,0}$, and $C_{2,2}$ as *a priori* with all other coefficients assumed to be initially zero. Our solutions included a 3×3 model, a 4×4 model, and one 4×4 solution that included the $C_{2,1}$ and $S_{2,1}$ coefficients that had not been

Table 3
Solutions for *GM* and normalized gravity field. All the MESSENGER solutions involved free adjustments of the parameters, including orbit and gravity coefficients, except where values are not shown.

Solution	GM (km³ s⁻²)	$C_{2,0}$ (1.0×10^{-5})	$C_{2,2}$ (1.0×10^{-5})	$S_{2,2}$ (1.0×10^{-5})	Residual range at CA M1/M2 (cm/s)
Mariner 10	22032.08 ± 0.9	−2.68 ± 0.9	1.55 ± 0.8		
Flyby 1[a]	22032.08	−2.68	1.55		4.3
Flyby 2[a]	22032.08	−2.68	1.55		14.2
Flybys 1 and 2	22031.77 ± 0.07				1.9/5.5
Flybys 1 and 2	22031.81 ± 0.07	−0.94 ± 0.37	1.30 ± 0.28		2.1/3.0
Flybys 1 and 2	22031.77 ± 0.07	0.61 ± 0.41	1.31 ± 0.28	−0.62 ± 0.34	2.8/2.0

CA denotes closest approach.
[a] No adjustment of gravity coefficients.

Table 4
Values of *GM* and spherical harmonic solutions to degree and order 3 and 4. These solutions were constrained by the application of a standard deviation for the *a priori* value of the coefficient. The standard deviation (σ) of each gravity coefficient is the formal value based on a data weight of 1 cm/s and needs to be calibrated downward. The rms is the root mean square of the fit to the full data set at 10-s rate; rge is the range of residuals around closest approach for flybys 1 and 2. For HgM001, $C_{2,1}$ and $S_{2,1}$ were set to zero and not estimated, whereas they were estimated for HgM001A.

	A priori value	A priori σ	3 × 3 solution	3 × 3 σ	HgM001		HgM001A	
					4 × 4 solution	4 × 4 σ	4 × 4 solution	4 × 4 σ
GM	22031.81	10,000	22031.79	0.08	22031.80	0.08	22031.80	0.08
$C_{2,0}$	−0.94	5.0	−0.940	0.9	−0.857	1.8	−0.842	1.8
$C_{2,1}$	0	5.0	0	0	0	0	−0.194	4.7
$C_{2,2}$	1.30	5.0	1.195	0.5	1.258	0.7	1.242	0.8
$C_{3,0}$	0	2.2	0.051	2.2	0.049	2.2	0.052	2.2
$C_{3,1}$	0	2.2	−0.621	1.2	−0.634	1.4	−0.617	1.4
$C_{3,2}$	0	2.2	0.289	2.1	0.098	2.2	0.085	2.2
$C_{3,3}$	0	2.2	−0.424	0.3	−0.403	0.4	−0.394	0.4
$C_{4,0}$	0	1.1			0.031	1.0	0.029	1.0
$C_{4,1}$	0	1.1			0.033	1.0	0.031	1.0
$C_{4,2}$	0	1.1			0.027	1.0	0.020	1.0
$C_{4,3}$	0	1.1			0.084	1.0	0.085	1.0
$C_{4,4}$	0	1.1			0.136	0.3	0.134	0.3
$S_{2,1}$	0	5.0			0	0	−0.176	4.7
$S_{2,2}$	0	5.0	−0.112	0.6	−0.043	0.9	−0.060	0.9
$S_{3,1}$	0	2.2	−0.427	1.2	−0.336	1.4	−0.340	1.5
$S_{3,2}$	0	2.2	0.162	2.1	−0.059	2.2	−0.071	2.2
$S_{3,3}$	0	2.2	0.012	0.4	−0.019	0.5	−0.021	0.5
$S_{4,1}$	0	1.1			0.036	1.0	0.037	1.0
$S_{4,2}$	0	1.1			−0.028	1.0	−0.032	1.0
$S_{4,3}$	0	1.1			−0.013	1.0	−0.012	1.0
$S_{4,4}$	0	1.1			−0.046	0.4	−0.044	0.4
rms			0.287		0.284		0.284	
rge			1.1; 1.4		0.87; 1.10		0.88; 1.11	

Units: *GM*, σ_{GM} are in km³ s⁻²; all coefficients and standard deviations are ×10⁻⁵; rms is in mm/s; rge is in cm/s.

included in any of the other solutions. These two coefficients represent the orientation of the angle between the polar axis of the coordinate system and the rotation vector. It was reasonable to assume that our data, which were largely near the equator, would have little sensitivity to the orientation of Mercury's spin axis, and so these quantities were omitted in most of our solutions, essentially assigning them a value of zero. The inclusion of these terms in one solution was an attempt to demonstrate our insensitivity to these terms through their estimated standard deviations.

Further, we added a constraint to the solutions because of the increased number of parameters being estimated. This constraint consisted of *a priori* standard deviations for all the coefficients that followed a Kaula (1966) rule for spherical harmonic degree *l* of $2 \times 10^{-4}/l^2$. Thus, the *a priori* standard deviations for all degree-2 terms were 5×10^{-5}, for all degree-3 terms were 2.2×10^{-5}, and for all degree-4 terms were 1.1×10^{-5}. This constraint ensured that the estimated coefficients would not deviate markedly from their *a priori* values unless the data strongly supported a different value.

The three spherical harmonic solutions are shown together with the *a priori* values and their *a priori* standard deviations in Table 4. The solutions all provide essentially the same value for *GM* and yield values very close to those shown in Table 4 for the degree-2 solutions. The *a priori* standard deviations for all the degree-2 coefficients suggest that they were able to adjust freely, and that the final formal uncertainty was significantly reduced from its *a priori* value with the exception of $C_{2,1}$ and $S_{2,1}$, for which the uncertainty hardly changed, as was expected. In contrast, most degree-3 and -4 coefficients have final standard deviations that are almost the same as the *a priori* values, suggesting that there is very little information about these coefficients in the data. The major exceptions are the $C_{3,3}$ and $C_{4,4}$ terms, which have half wavelengths, respectively, of 60° and 45° in longitude and latitude.

The best solution overall is 4 × 4 HgM001 because it better represents the data near closest approach in residual range and root mean square (rms) residual. Including the (2, 1) coefficients in HgM001A makes no improvement. The 3 × 3 solution is almost as good on the basis of the above criteria of rms and range, and its values for the degree-2 coefficients and *GM* are the same within any reasonable error estimate as for HgM001. Estimating additional coefficients of degrees 5 and 6 produced no measurable improvement in the solution.

The main surprise from these solutions is the small value of $C_{2,0}$, approximately one third of the *a priori* value from Mariner 10, which is problematic with regard to geophysical interpretation, as discussed in Section 5.2. The calibration of the standard deviations for the gravity coefficients is therefore important in the context of understanding whether the difference in $C_{2,0}$ between MESSENGER and Mariner 10 is of significance. First, we attempted to estimate the influence of the length of the data span on the results by redoing the HgM001 solution using smaller data sets of 6, 8, 10, 12, and 14 days. In these solutions all *a priori* values were identical. We used the same constraint model as HgM001, and the initial gravity field and *GM* were from the Mariner 10 solution. The 14-day arc is different from HgM001, which is also 14 days, because the *a priori* value in HgM001 was an earlier 2 × 2 solution (Table 3). Each solution was iterated once. We also constructed two additional solutions with fixed values of $C_{2,0}$ to see if a different value for $C_{2,0}$ could lead to an equally acceptable solution for the other degree-2 coefficients, $C_{2,2}$ and $S_{2,2}$, with the latter expected to be identically zero. These solutions were also 4 × 4 and constrained in the same way as HgM001.

These solutions for different data set lengths and with fixed $C_{2,0}$ values are shown in Fig. 7. The solutions with fixed $C_{2,0}$ ($J_2 = 6, 5$, and 4×10^{-5}) are shown on the left side of the chart. The rms fit to the entire data set was not substantially changed, but the value of $S_{2,2}$, which is expected to be zero, is very large. The values of $C_{2,2}$ are acceptable and are reasonably stable. If these results are extrapolated they almost intersect with the HgM001 values, shown
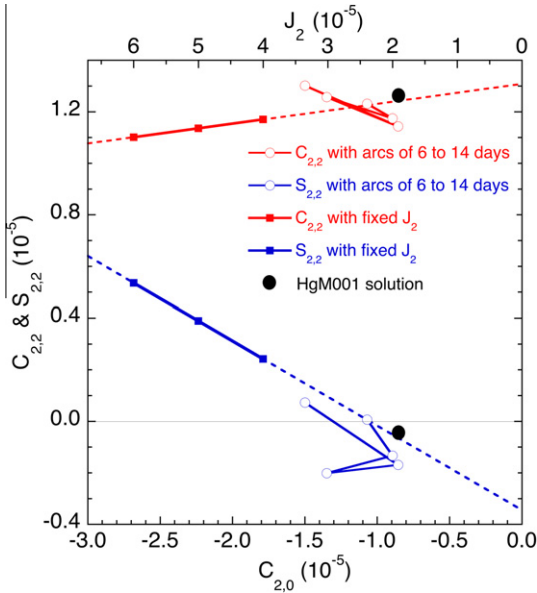
Fig. 7. Results for $C_{2,0}$, $C_{2,2}$ and $S_{2,2}$ from a series of 4×4 gravity field solutions for fixed values of $C_{2,0}$ and for data sets varying in length from 6 days to 14 days. The extrapolation of the solutions with fixed J_2 leads to the HgM001 values indicating linearity in the solution adjustment. The solutions for various data lengths are all grouped together, and all started from the M10 values for gravity with consistent *a priori* values for the other parameters.

on the figure. Thus, if we were to accept a larger value of $C_{2,0}$ than the MESSENGER data indicate, a larger $S_{2,2}$ value is needed.

The result of changing the arc length of the data set is also shown in Fig. 7. The five values are grouped in a relatively small area, suggesting that the data span is not the cause of the low value of $C_{2,0}$. The change in $S_{2,2}$ is greater than that of $C_{2,2}$, suggesting that the latter is relatively well determined and we can use the spread of values as a way of estimating the scaling factor and true standard deviation of the HgM001 coefficients. From the variation in the length of data set we obtain standard deviations of 0.28×10^{-5} for the mean for $C_{2,0}$, 0.063×10^{-5} for $C_{2,2}$, and 0.12×10^{-5} for $S_{2,2}$, which are 1/6, 1/11, and 1/7 of the formal standard deviations.

Another way of estimating the real errors is by looking at the sizes of the estimated coefficients that are expected to be zero: $S_{2,2}$, $C_{2,1}$, and $S_{2,1}$. If we wish a standard deviation to be three times the estimated coefficient value, then the standard deviation of $S_{2,2}$

in HgM001A in Table 4 would be 0.18×10^{-5}, or 1/5 of the formal value in the table. For $C_{2,1}$ and $S_{2,1}$, the ratios (3 × coefficient magnitude)/(formal standard deviation) are both 1/8. From these results, we assume that a representative scale factor for the formal standard deviations is 1/6. Applying this factor to the HgM001 solution, we obtain for the main (normalized) coefficients

$C_{2,0} = (-0.86 \pm 0.30) \times 10^{-5}$; equivalent to
$J_2 = (1.92 \pm 0.67) \times 10^{-5}$,
$C_{2,2} = (1.26 \pm 0.12) \times 10^{-5}$; equivalent to an unnormalized
$C_{2,2} = (0.81 \pm 0.08) \times 10^{-5}$,
$S_{2,2} = (-0.04 \pm 0.15) \times 10^{-5}$.

$$(2)$$

The above standard deviations do not explain the difference in $C_{2,0}$ from the M10 estimate, even if we consider them to be 1-σ values. The scaling of the formal error estimate for GM is probably 1/2, even though it was one of the most stable parameters throughout the analysis. Thus our estimate for GM is

$$GM = 22031.80 \pm 0.04 \text{ km}^3 \text{ s}^{-2}. \qquad (3)$$

The possibility of a systematic error in the solution cannot be ignored and is one of the reasons that we studied the separability of GM and $C_{2,0}$ (see Fig. 7).

The correlations for the HgM001 solution, which are generally small except for certain coefficient pairs, notably $C_{2,0}$ with $C_{4,0}$ and $S_{2,2}$, $C_{2,2}$ with $C_{4,2}$, and $S_{2,2}$ with $S_{4,2}$, and several degree-3 coefficients, are shown in Fig. 8. However, at least one coefficient in any pair is usually small, suggesting that the effect of the correlation is probably not important. The tradeoff between $C_{2,0}$ and $S_{2,2}$ is quantified in Fig. 7.

Another consideration in the reliability of the results is the degree of convergence of the solution. In Table 4 the solutions were iterated at least twice by changing the *a priori* gravity field and re-estimating all the parameters. In Fig. 7, all solutions started from the Mariner 10 values and were iterated once after convergence of the trajectory parameters. The difference between the iterated HgM001 solution shown in the chart and the extrapolated solutions with fixed J_2 or varying arc lengths (only one solution had the same data span as HgM001) after one iteration is relatively small and does not change the general result. The subject of convergence is raised only because the flyby trajectories are not closed orbits about Mercury (as they will be after orbit insertion in 2011)

	C2,2	C3,0	C3,1	C3,2	C3,3	C4,0	C4,1	C4,2	C4,3	C4,4	S2,2	S3,1	S3,2	S3,3	S4,1	S4,2	S4,3	S4,4	GM
C2,0	0.18	0.20	-0.16	0.15	-0.17	0.70	0.07	0.03	0.04	0.12	-0.62	0.33	-0.09	-0.23	0.04	-0.46	-0.05	-0.09	0.01
C2,2		0.05	-0.25	0.35	0.04	-0.05	-0.03	0.61	0.01	0.07	-0.12	0.15	-0.18	-0.21	-0.02	-0.02	0.03	-0.12	0.11
C3,0			0.07	-0.01	-0.00	-0.03	-0.01	0.00	-0.01	0.00	-0.09	0.06	0.01	0.03	-0.01	0.02	0.01	0.01	-0.02
C3,1				0.00	0.58	0.06	0.08	-0.11	0.04	0.08	0.07	-0.84	-0.10	0.64	0.09	-0.07	0.02	0.30	-0.01
C3,2					0.05	-0.02	-0.01	-0.05	0.00	-0.10	0.06	-0.01	-0.01	0.00	0.00	-0.01	-0.00	0.21	0.14
C3,3						-0.01	0.06	0.11	0.50	-0.01	0.07	-0.52	0.05	0.30	0.12	0.14	-0.12	0.19	-0.05
C4,0							-0.01	-0.01	-0.00	-0.05	-0.19	-0.01	0.01	0.02	-0.01	0.05	0.01	0.01	0.10
C4,1								0.00	-0.00	0.00	0.00	0.06	0.01	-0.12	-0.01	0.00	0.00	0.00	0.04
C4,2									0.01	0.04	-0.01	-0.11	-0.01	-0.16	0.01	-0.01	-0.00	0.38	0.08
C4,3										-0.01	-0.05	0.06	0.01	0.09	-0.01	0.01	-0.00	-0.05	0.01
C4,4											0.08	0.00	-0.21	0.01	-0.02	-0.39	0.05	-0.01	0.16
S2,2												-0.25	0.32	0.31	-0.03	0.56	0.03	0.22	0.22
S3,1													-0.09	-0.60	0.16	-0.00	-0.01	-0.41	0.01
S3,2														-0.00	0.01	-0.04	-0.00	-0.05	0.09
S3,3															0.08	-0.01	0.42	0.35	-0.16
S4,1																0.00	0.00	0.03	0.03
S4,2																	-0.00	0.01	0.04
S4,3																		0.01	-0.04
S4,4																			-0.06

Fig. 8. Correlation matrix for the HgM001 solution. The correlations between GM and all gravity coefficients are small; the correlations with $C_{2,0}$ are large only for $C_{4,0}$, $S_{2,2}$, and $S_{4,2}$. All correlations >0.5 have colored backgrounds.
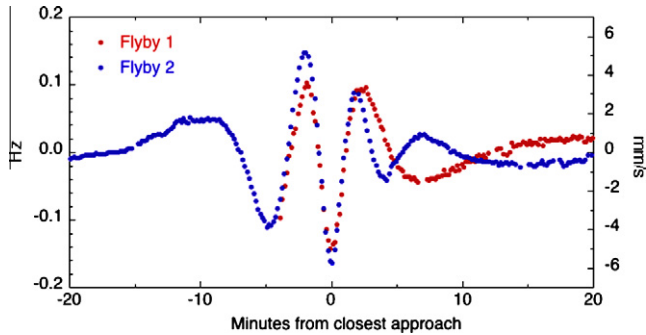
Fig. 9. Doppler residuals from the HgM001 gravity model near closest approach. Although the signatures are similar for the two flybys, the ground tracks are nearly 180° apart in longitude. For flyby 1 the residuals are mostly the along-track velocity component, and for flyby 2 they are nearly radial to the orbit. The data are at 10-s rate, and the Doppler noise is ∼0.1 mm/s.

and thus are potentially vulnerable to changes in the trajectory from iteration to iteration.

The final consideration in understanding our solutions is that the HgM001 solution does not fully satisfy the Doppler tracking data (Table 4). Thus some gravity signal remains in the data that we have not recovered. The Doppler residuals for the flybys are shown in Fig. 9 with respect to the time of closest approach. The residual patterns in Fig. 9 show a small perturbation of the spacecraft velocity over a 20-min period that we have not modeled. The structure of the residual patterns around closest approach is similar for the two encounters, but the longitudes of closest approach to Mercury during flybys 1 and 2 were on opposite sides of the planet. In addition, the residuals (in the direction of Earth) are along-track on flyby 1 and nearly radial to Mercury on flyby 2.

The displacement of the spacecraft center of mass from its mean position in the orbit during flyby 2 at closest approach is in the direction of line-of-sight to Earth, which is largely in the radial direction from Mercury. The magnitude of the displacement is approximately ±25 cm and is small compared to the size of the MESSENGER spacecraft. Conceivably, this displacement could be the result of incorrect modeling of the spacecraft attitude, position of the center of mass of the spacecraft, and/or motion of the phase center of the antenna during the flyby, although we do not think that any of these are the explanation.

The implied accelerations of the displacement that occur within a 5-min period are approximately ±4 mGal, and the possibility that this residual signal could be explained by the presence of one or more surface mass anomalies near the ground track of the spacecraft is discussed briefly in the next section.

The gravity anomalies for the HgM001 gravity model are shown in Fig. 10. The top chart shows positive anomalies at 0/360° longitude and at 180°, and negative anomalies near 120°E and 240°E longitude, revealing the elliptical gravitational shape of the equator. The center chart shows the anomalies when $C_{2,2}$ is assumed zero but all other coefficients are the same, representing the anomalous gravity field that is not explainable by the triaxial geoidal shape of the body. Note that a large positive gravity anomaly is seen at about 70°E and a negative anomaly at about 230°E. Further, there is some suggestion of positive gravity at 0°E and 180°E even after removal of the $C_{2,2}$ term.

The lower chart in Fig. 10 shows the predicted errors in the anomalies for a scaling of the formal errors by 1/6 and the correlations shown in Fig. 8. As expected, greater accuracy is seen along the ground track of both flybys at about 2 mGal. It is important to remember that the ability to assign anomalies to the north or south is difficult with near-equatorial data. Thus, the large negative anomalies at high latitudes and longitudes 30–90°E could be in both hemispheres as the chart suggests, or in either one.

4.2. Gravity anomaly solutions and large basins

In an effort to fully satisfy the Doppler signal we obtained a series of gravity field solutions that included a single adjustable surface mass anomaly as well as 4×4 spherical harmonics. In preliminary analysis we had found that a set of regularly spaced $10° \times 10°$ surface mass anomalies alone was not able to satisfy the Doppler data as well as a 4×4 gravity field. Thus, we used the HgM001 solution as the *a priori* gravity field and estimated a new 4×4 gravity field simultaneously with a $10° \times 10°$ degree surface mass anomaly in a given location. Because of the possibility that Mercury might have mascons (large positive mass anomalies associated with impact basins), like the Moon (Muller and Sjogren, 1968) and Mars (Smith et al., 1999), we chose the anomaly locations to be major basins on Mercury that had been previously identified from Mariner 10 (Spudis and Guest, 1988) and MESSENGER images (Watters et al., 2009). In each case the *a priori* value of the anomaly was zero, and the *a priori* standard deviation was 10 mGal.

We estimated a $10° \times 10°$ anomaly in each of 24 of the larger basins distributed across the planet and used the range of residuals near closest approach on each flyby as a measure of the importance of a given location. A new 4×4 spherical harmonic solution was obtained with each gravity anomaly.

In general, the allowance for mass anomalies at all locations made a small improvement to the magnitude of the residual pattern. The M1 residual spread was reduced from 8.72 mm/s for HgM001 to about 8.30 mm/s for 22 of the 24 basins, and for M2 was reduced from 11.08 mm/s to about 10.85 mm/s. Because we obtained similar results for all basins, we believe the reduction was probably the result of adding an additional variable to the solution and purely a numerical effect. The values of the anomalies were generally a few tenths of mGal, and the estimated standard deviation was only slightly less than the *a priori* standard deviation.

One surface mass anomaly made a larger residual reduction, from 8.72 to 8.02 mm/s on flyby 1 and 11.08 to 9.77 mm/s on flyby 2. This anomaly was located at the Mena-Theophanes basin (centered at 1°S, 231°E). This basin (Spudis and Guest, 1988; Table II) was partly mapped by Schaber et al. (1977) and analyzed in greater detail by Spudis and Strobell (1984). Analysis of Earth-based radar altimetry by Harmon et al. (1986) showed that, although evidence of a topographic rim could be found along several parts of the basin's circumference, the interior is not markedly lower than the surrounding terrain. Harmon et al. (1986) concluded that although the radar data did not offer unambiguous support that this feature is a multi-ringed basin, if it is of impact origin the topography suggests that the basin interior was highly modified, perhaps by volcanic fill. The magnitude of the surface mass anomaly at Mena-Theophanes in our solution was −0.9 ± 0.5 mGal, after scaling (i.e., a mass deficiency). This basin is located in a region of negative gravity anomaly in Fig. 10 and along the M2 ground track, accounting for the greater reduction in residuals for flyby 2 than for flyby 1. The revised gravity anomaly map is shown in Fig. 11 and should be compared with the top chart in Fig. 10; note that the figure scales are slightly different. The results are consistent with a mass anomaly in this region that contains non-negligible contributions at wavelengths shorter than degree 4.

One result of solving for the surface mass anomaly was to increase the global anomaly range to 40 mGal from 35 mGal for HgM001, although the value at the Mena-Theophanes location was almost unchanged at approximately −12 ± 2 mGal. We compared the magnitude range of anomalies for HgM001 (±18 mGal) with a 4×4 gravity model of the lunar nearside where there are several mascons, although they are not resolvable in a 4×4 lunar gravity model.
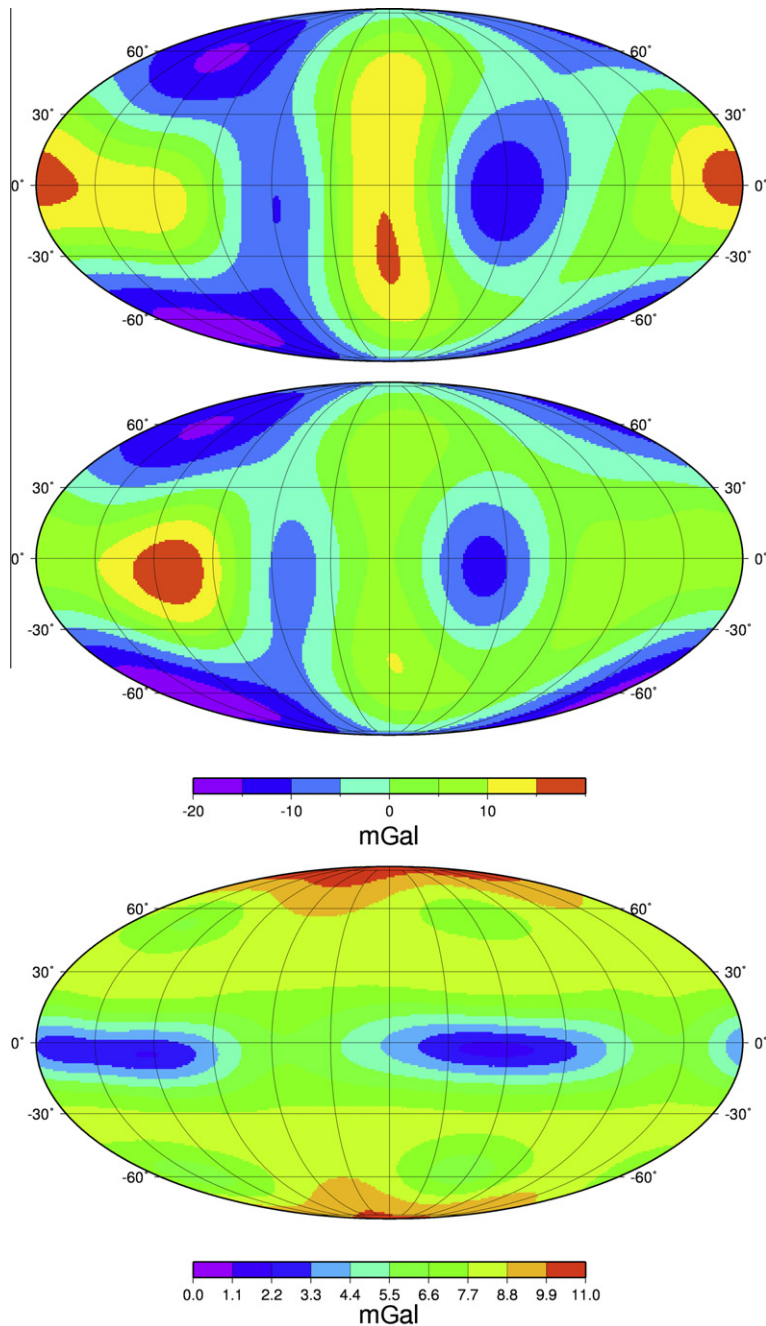
Fig. 10. HgM001 gravity anomaly and error maps in Mollweide projection centered on longitude 180°E. Top: gravity anomalies. Middle: gravity anomalies with $C_{2,2} = 0$. Bottom: estimated errors based on a scaling of 1/6 of the formal errors. Top chart shows the triaxial gravitational shape of Mercury; middle chart shows anomalous gravity when the gravitational equatorial ellipticity is set to zero; bottom chart shows the estimated errors in both the above fields. Note that the scale for the bottom chart is different from those for the top and middle charts.

The lunar nearside gravity, at 4 × 4 resolution, has an anomaly range of −15 to +30 mGal, which is a ~25% larger range than we see on Mercury. We compared only the front side of the Moon with HgM001 because South Pole-Aitken and the adjacent highlands dominate the Moon's farside gravity field even at these wavelengths and display an anomaly range of over 100 mGal. The inability to recover anomalies at the selected impact basins does not therefore imply that Mercury does not possess large mass concentrations. We consider the question open and unanswerable with the flyby data alone.

Although the estimation of the surface mass anomaly made a relatively large reduction (~10%) in the residual patterns, the new 4 × 4 gravity model had a numerically smaller value of $C_{2,0}$ and a larger $S_{2,2}$, making the solution less physically acceptable. It appears that estimating a gravity anomaly close to the equator has the consequence of reducing the gravitational flattening and changing the equatorial ellipticity. However, there was no major change in the value of $C_{2,2}$. Of probably greater importance is the change in the anomaly map of HgM001 (Fig. 10, top, to Fig. 11) as a result of adding a single anomaly to the solution. This change reflects the remaining Doppler residuals and the overall sensitivity of the solution from the data on these two flybys. Thus we did not pursue adjusting any additional anomalies and consider the HgM001 model as the preferred model overall.
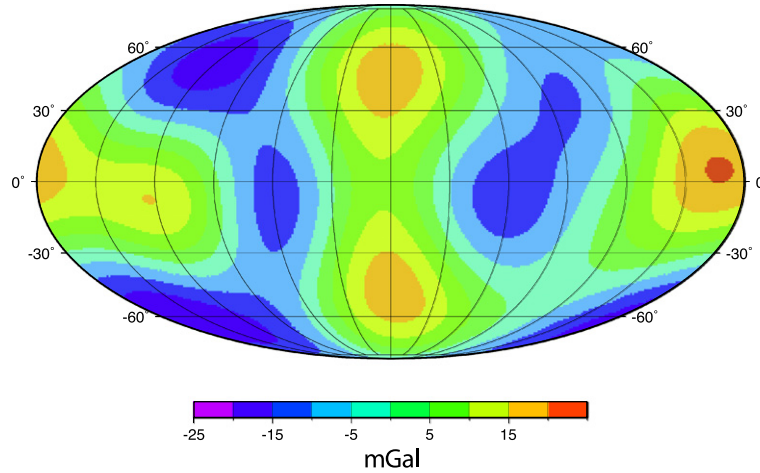
Fig. 11. Gravity anomalies for a 4 × 4 spherical harmonic model plus a single gravity anomaly at −1°S, 231°E, in the region of the Mena-Theophanes impact basin. This figure should be compared with the top chart in Fig. 10. Note the different scales on the two maps.

A second basin, Tolstoj (16.4°S, 195.2°E), also produced a slightly greater reduction in residual spread than the majority, to 8.24 and 10.51 mm/s for flybys 1 and 2, respectively, with a magnitude of +1.4 ± 1.5 mGal after scaling. The Tolstoj basin is in an area of positive gravity anomaly in Fig. 10. Tolstoj is also closer to the ground track of M2 than that of M1, but it is still more than 400 km south of the flyby 2 ground track.

Finally, it is recognized that the altitude of the spacecraft limits the resolution of the gravity field that can be resolved on the surface. Generally, horizontal resolution is usually limited to about half the altitude. At closest approach, MESSENGER was 200 km above the surface, so the resolution would be about 100 km, or about 2.5°, at this location. For an anomaly located 30° of arc from the track, the range from 200 km altitude would be about 1300 km and the resolution 650 km or 16°. At 1000-km altitude and at a horizontal offset of 45° of arc, the resolution is 30°, corresponding to spherical harmonic degree and order 6.

So MESSENGER is probably sensitive to anomalies of degree and order 6 and higher (equivalent to over 100 gravity coefficients) during the flyby, but our data set is able to support only a fraction of this number in an inversion solution. HgM001 has 19 coeffi-

cients, even when we apply a constraint. Thus MESSENGER is sensitive to more gravity parameters than the flyby data are able to resolve.

5. Implications for internal structure

5.1. Constraints on crustal structure from equatorial altimetry and gravity

If the mean crustal thickness is small relative to the planetary radius, then from the geometric description of equatorial shape presented in Section 4, the difference in crustal thickness between the first and third quadrant is approximately (Kaula et al., 1972) $2F_1(\Delta\rho/\bar{\rho})$. Here $\Delta\rho$ is the density contrast between the crust and the average density of the remainder of the planet, and $\bar{\rho}$ is the planetary mean density. With the approximation $\Delta\rho/\bar{\rho} \approx 0.5$, the difference in crustal thickness is only about 3 km. This result suggests that a simple crustal thickness difference does not explain the gravity and shape, and additional investigation into implications for internal structure is warranted.

In Section 4 we presented results indicating that the estimated gravity coefficient $S_{2,2}$ is essentially zero in our preferred gravity model, HgM001, indicating that Mercury's coordinate system is aligned along its principal inertia axes. This is precisely what is expected because of the planet's 3:2 spin orbit resonance, which orients the minimum moment of inertia axis towards the Sun at perihelion (Colombo, 1965; Goldreich and Peale, 1966), and because 0° and 180° longitudes correspond to noon at perihelion (the so-called "hot poles"). The fact that the orientation of the long axis of the shape ellipse, φ_2, is close to 0° suggests that the equatorial gravitational moments have a causative relationship to the equatorial shape. Specifically, $C_{2,2}$ and the equatorial moment difference $(B - A)$ must be strongly controlled by the elliptical (degree-2) shape plus any interior density boundaries that are correlated with this shape. Examples could be the crust/mantle and core/mantle boundaries, and/or degree-2 density variations within the mantle (e.g., from convection or melt depletion). An interesting question is the historical relationship between the equatorial degree-2 shape and orientation of the planet, and whether there has been "equatorial wander" in the 3:2 resonance state. We first evaluate whether the equatorial shape alone can properly account for the equatorial moments using the relationship (Zuber et al., 2008):
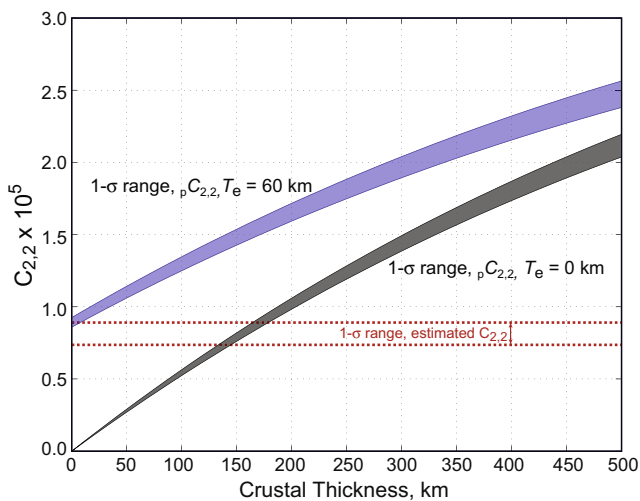

Fig. 12. Estimated and modeled gravity coefficient $C_{2,2}$ as a function of crustal thickness. At zero crustal thickness, the model results provide an upper bound on elastic thickness for the adopted parameter set (see Section 5.1). The upper bound on crustal thickness occurs for zero elastic thickness.

$$(B - A) = \frac{2}{5} \frac{\rho_c}{\bar{\rho}} MR(a - b), \tag{4}$$

where R, M, and ρ_c are Mercury's mean radius, mass, and crustal density, respectively. With the combined MLA-radar $(a - b)$ value of 1555 ± 341 m and $\rho_c = 3000$ kg m^{-3}, the $(B - A)$ prediction is $(2.770 \pm 0.607) \times 10^{32}$ kg m^2. The estimated $(B - A)$ moment difference is obtained from the estimated $C_{2,2} = (0.81 \pm 0.08) \times 10^{-5}$, using $C_{2,2} = (B - A)/4MR^2$, and is $(0.640 \pm 0.061) \times 10^{32}$ kg m^2. Obviously, this discrepancy requires substantial compensation of the degree-2 equatorial shape. Although the planetary density distribution that gives rise to the equatorial moments cannot be determined uniquely, it is reasonable to explore a model composed of the surface topography and a partially to fully compensated crust–mantle boundary (e.g., Anderson et al., 1996). Here the relationship between the predicted gravity coefficient, $_pC_{2,2}$, and the shape coefficients, $c_{2,2}$ and $s_{2,2}$, is:

$$_pC_{2,2} = \frac{3}{5} \frac{\rho_c}{\bar{\rho}} \frac{1}{R} \left\{ 1 - C_2 \left(\frac{R_c}{R} \right)^4 \right\} \sqrt{c_{2,2}^2 + s_{2,2}^2}, \tag{5}$$

where R_c is R minus the mean thickness of the crust, h_c. Here C_2 is the "degree of compensation" (and the term in brackets is the "isostatic response function") for spherical harmonic degree $l = 2$. Given the estimated gravity and topography coefficients, specification of ρ_c and C_2 provides an estimate of the crustal thickness h_c. Setting C_2 to 1 corresponds to perfect isostatic compensation by mass balance. Anderson et al. (1996) used this approach for Mercury and obtained $h_c = 203 \pm 101$ km for $\rho_c = 3000$ kg m^{-3}, which with our gravity and topography coefficients yields $h_c = 156 \pm 23$ km. This new result is within the uncertainty in the Anderson et al. (1996) estimate but carries an error four times smaller.

However, simple mass balance is not a good approximation for compensation of the shape because membrane stresses can provide an important support of topography at degree 2 (Turcotte et al., 1981). The l-dependent degree of compensation for flexural and membrane support is a function of ρ_c and the mantle density, ρ_m; Young's modulus, E, and Poisson's ratio, v; and the effective elastic thickness of the lithosphere, T_e. Adopting a parameter set $\rho_c = 3000$ kg m^{-3}, $\rho_m = 3500$ kg m^{-3}, $E = 50$ GPa, $v = 0.25$, and $T_e = 60$ km yields $C_2 = 0.747$, indicating that a less than equivalent interior mass (opposite in sign) in conjunction with membrane stresses would support the surface mass associated with the degree-2 shape. As T_e approaches 0, C_2 converges to 1, the mass balance solution; as T_e increases, $_pC_{2,2}$ increases to the point where it lies above the estimated range of $C_{2,2}$ for a given h_c. This relation provides an upper bound on T_e at the limit of zero crustal thickness, as illustrated in Fig. 12, which shows predictions for $T_e = 0$ km and 60 km.

Given that the gravity constraint, $C_{2,2}$, produces a spectrum of solutions for h_c as a function of T_e, refinement of crustal thickness knowledge can be achieved with independent information on this elastic parameter. Nimmo and Watters (2004) estimated that at the time of fault slip on one lobate scarp on Mercury, T_e was 25–30 km. This local result was based on a depth of faulting on the thrust fault thought to underlie the lobate scarp of 30–40 km (Watters et al., 2002; Zuber et al., 2010). The depth of faulting was equated to the depth of the brittle–ductile transition, and this depth was converted to T_e by the usual moment–curvature procedure (McNutt, 1984). Fig. 13 shows the h_c solution space for a wide range of E and ρ_c values and adopts the T_e estimate, 25 km, and the assumed mantle density, 3300 kg m^{-3}, of Nimmo and Watters (2004). Adopting their values of E and ρ_c for self-consistency yields $h_c = 30$ km. In general, the solutions would seem to cover broad parameter ranges, but additional considerations can limit the possibilities. The bulk of Mercury's crust likely formed through re-
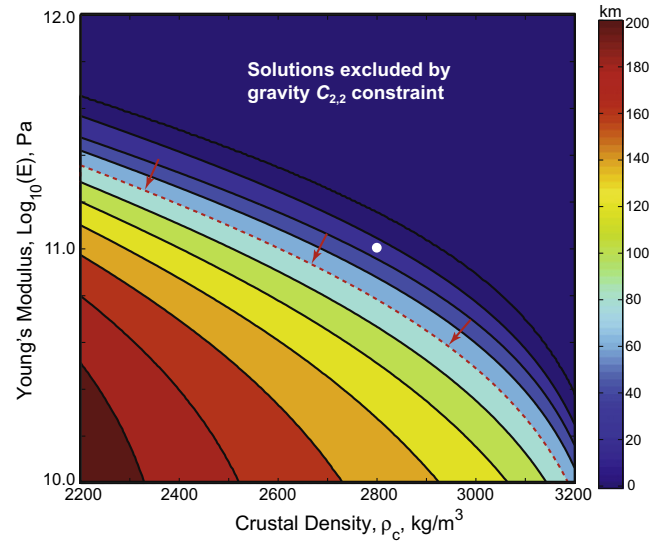

Fig. 13. Solution space of crustal thickness, h_c, as a function of E and ρ_c, using the estimated T_e of 25 km and assumed $\rho_m = 3300$ kg m^{-3} from Nimmo and Watters (2004). Contour interval is 20 km, from 0 to 200 km. The dark blue area, which cannot physically satisfy the $C_{2,2}$ constraint ($h_c < 0$), is excluded. The white dot is the solution for the parameter values of Nimmo and Watters (2004), and the red dashed line is their upper bound on crustal thickness derived from a lower-bound crustal solidus temperature of 1400 K.

peated volcanic activity, and there is essentially no evidence for an early feldspar-rich flotation crust similar to the lunar highlands (Denevi et al., 2009). This finding indicates that the upper range of crustal densities in Fig. 13 is more likely, though stronger constraints on crustal density should be forthcoming from the MESSENGER mission orbital phase. For values of E greater than 50 GPa, this mild density constraint limits the solution space for h_c to not much greater than $\sim$100 km. Independently, a requirement that the crustal base temperature not exceed the solidus temperature limits crustal thickness to $\sim$80–100 km for a solidus temperature range of 1400–1600 K (Nimmo and Watters, 2004). Thus thermal, tectonic, and MESSENGER shape/gravity analyses tell a consistent story of a crust likely no more than 100 km thick.

5.2. Implications of gravity for core state

Mercury is in Cassini state 1, where the spin axis, the orbit normal, and the normal to the Laplace plane remain coplanar as the first two vectors precess around the latter at a current instantaneous rate corresponding to a period of 328,000 years (Peale, 1976; Peale et al., 2002; Margot et al., 2007). Occupancy of the Cassini state leads to the expression,

$$\frac{C}{MR^2} = \frac{\left[\frac{J_2}{(1-e^2)^{3/2}} + 2C_{2,2} \left(\frac{7}{2} e - \frac{123}{16} e^3 + O(e^5) \right) \right] \frac{n}{\mu}}{(\sin I)/i_c - \cos I}, \tag{6}$$

where $A < B < C$ are the principal moments of inertia, with C being the moment of inertia about the spin axis; i_c is the obliquity of Cassini state 1 (and is equal to Mercury's obliquity); e is the eccentricity of Mercury's orbit; I is the inclination of Mercury's orbit plane to the Laplace plane on which Mercury's orbit precesses with approximately constant inclination; n is the orbital mean motion, and μ is the frequency of the orbit precession.

Mercury's obliquity, $i_c = 2.11 \pm 0.1$ arcmin (Margot et al., 2007), is known much more precisely than either J_2 or $C_{2,2}$, which allows us to write J_2 as a function of $C_{2,2}$ for particular values of C/MR^2 from Eq. (6). This exercise has been carried out in Fig. 14 for the likely extreme values of C/MR^2 (Harder and Schubert, 2001; Hauck
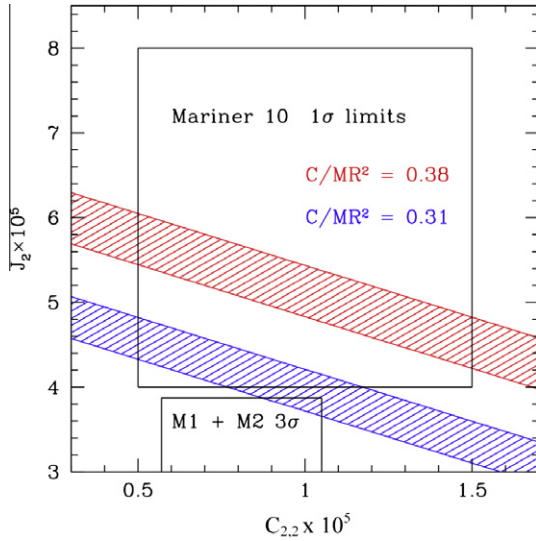
Fig. 14. Observational constraints on J_2 and $C_{2,2}$. Values admitted by the obliquity measurement and the occupancy of the Cassini state are computed for two extreme values of C/MR^2 according to Eq. (6) and shown by the color bands. The vertical spread of the color bands corresponds to the 1-σ uncertainty in the measured obliquity. The spread in the values admitted from analysis of radio science data from three Mariner 10 flybys and two MESSENGER flybys are shown by boxes corresponding to 1-σ and 3-σ, respectively. The current estimate of J_2 from MESSENGER data appears to be overly small (see text).

Fig. 15. Distribution of C_m/C implied by the normal distributions in $(B - A)/C_m = (2.03 \pm 0.12) \times 10^{-4}$ and $(B - A)/MR^2 = (3.24 \pm 0.32) \times 10^{-5}$ and two extreme values of C/MR^2, 0.31 and 0.38. The distributions are based on Eq. (7).

et al., 2007). (Note that C/MR^2 increases with the sulfur content of the core; the lower bound corresponding to 0% sulfur was used by both Harder and Schubert and by Hauck et al., and the upper bound corresponds to 35% sulfur, from Harder and Schubert.) The vertical range of the bands for each value of C/MR^2 corresponds to the 1-σ extremes in i_c. Also in Fig. 14 are boxes showing the 3-σ extremes for the two MESSENGER flybys and the 1-σ extremes for the Mariner 10 values (Anderson et al., 1987). The HgM001 MESSENGER gravity model gives the unnormalized coefficients $J_2 = (1.92 \pm 0.65) \times 10^{-5}$ and $C_{2,2} = (0.81 \pm 0.08) \times 10^{-5}$. Because both flybys were near-equatorial, the sensitivity to $C_{2,2}$ is much greater than that for J_2 (Section 4.1). If we substitute these values of J_2 and $C_{2,2}$ along with the value of i_c in Eq. (6), the 1-σ extremes in these variables lead to $0.122 < C/MR^2 < 0.228$. Both of these limits are considerably less than the smallest plausible values of the moment of inertia obtained by Harder and Schubert (2001) and Hauck et al. (2007) and shown in Fig. 14. This result implies that the more uncertain J_2 should be considerably larger than that obtained by the gravity field solution. A larger value of J_2 would raise the MESSENGER 3-σ box in Fig. 15 and make it more consistent with both the Mariner 10 value and the constraints imposed by the obliquity. Unfortunately, as discussed in Section 4.1, a higher value of J_2 provides a considerably poorer fit to the tracking data than the recovered solution; increasing J_2 to desired levels also results in a non-zero $S_{2,2}$, which is also quite problematic.

There is no analogous issue with the least-squares solution for $C_{2,2}$, which is well determined from the equatorial flyby geometry (Section 4.1). We can use the smaller uncertainty in this term to refine the constraints on C_m/C, where C_m is the polar moment of inertia of the mantle and crust alone. Following Peale et al. (2002) we write

$$\frac{C_m}{(B - A)} \frac{(B - A)}{MR^2} \frac{MR^2}{C} = \frac{C_m}{C}, \tag{7}$$

where $(B - A)/C_m = (2.03 \pm 0.12) \times 10^{-4}$ is determined from the amplitude of the physical libration in longitude (Margot et al.,
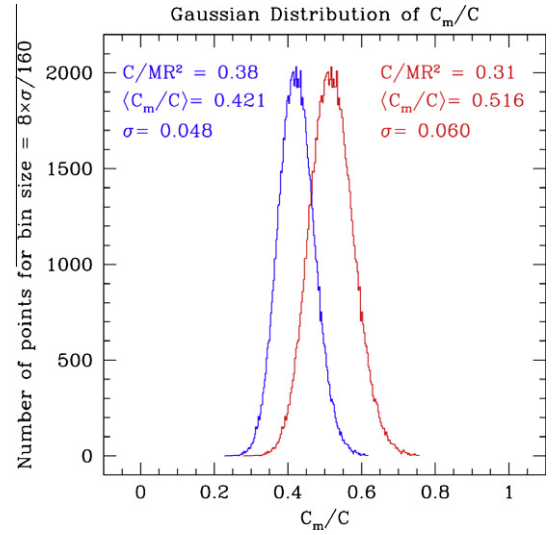
2007), and $(B - A)MR^2 = (3.24 \pm 0.32) \times 10^{-5} = 4C_{2,2}$. If we assume that $(B - A)/C_m$ and $(B - A)/MR^2$ are normally distributed with mean values and standard deviations as indicated, we can construct the distribution of C_m/C with random insertions into the normal distributions and for fixed extreme values of modeled C/MR^2. The distributions for the two extreme values of C/MR^2 are shown in Fig. 15. The mean value of C_m/C is near 0.5 for any value of C/MR^2 between the extremes, and the small σ between 0.053 and 0.060 means that the first two MESSENGER flybys have reinforced the conclusion of Margot et al. (2007) that Mercury's mantle is decoupled from a fluid outer core on the 88-day annual period of the forced libration. The value of $C_{2,2}$ would have to be increased by almost 9-σ to bring C_m/C near 1, the value this technique would find were the core solid. Reducing the uncertainty in C_m/C is one of the most important contributions from the two MESSENGER flybys of Mercury.

6. Summary

Altimetric and radio tracking observations from MESSENGER's first two flybys of Mercury have improved knowledge of the planet's equatorial shape and gravitational signature. During each flyby, MLA collected an altimetric pass that spanned about 3200 km along the planet's near-equatorial region. The passes were situated on opposite hemispheres of the planet, and they span collectively ~40% of the planetary circumference. The mean elevation of the M1 profile, in the longitude range 0–90°E, is greater than the mean of the M2 profile, in the longitude range 180–270°E, indicating an equatorial COF-COM offset as observed for other terrestrial planets (Wieczorek, 2007), with a magnitude in good agreement with analyses of Earth-based radar topography (Anderson et al., 1996). The MLA profiles both exhibit slopes of ~0.015° downward to the east, which is consistent with a long-wavelength equatorial shape defined by an ellipse.

Doppler tracking of the MESSENGER flybys from the radio-frequency tracking system (Srinivasan et al., 2007) shows great sensitivity to the gravitational structure of Mercury. The equatorial ellipticity, $C_{2,2}$, is well determined and correlates with the equatorial shape. The $S_{2,2}$ coefficient is ~0, as would be expected if Mercury's coordinate system is aligned along its principal axes of inertia. The recovered value of the polar flattening of the gravitational potential, J_2, is considerably lower in magnitude than the va-

lue obtained from Mariner 10 tracking (Anderson et al., 1996), a problematic result for internal structure models. This parameter is not as well constrained as the equatorial ellipticity, however, because the flyby trajectories were nearly in Mercury's equatorial plane. The residuals from the Doppler tracking data allow for the presence of mascons on Mercury, but flyby observations are of insufficient resolution for confident recovery.

The equatorial shape parameters $c_{2,2}$ and $s_{2,2}$ and the gravitational equatorial ellipticity $C_{2,2}$ collectively provide a constraint on crustal thickness from the equatorial topography and the extent of its compensation at a crust–mantle boundary. For various assumptions of degree of compensation and crustal and mantle density, the range of allowable crustal thickness in all plausible scenarios is consistent with the upper limit of about 100 km derived from the inferred depth of thrust faulting beneath a prominent lobate scarp, an assumed flow law for crustal material, and the condition that the crustal base temperature not exceed the solidus temperature (Nimmo and Watters, 2004).

The improvement in Mercury's equatorial gravitational ellipticity has allowed a markedly improved estimate of the ratio of the polar moment of inertia of the mantle and crust to the full polar moment (C_m/C). This refinement strengthens the conclusion of Margot et al. (2007) that Mercury presently has a fluid outer core.

Further observations from MESSENGER during the orbital phase of the mission beginning in March 2011 will improve substantially the altimetric and gravitational characterization of Mercury. This characterization will lead to a greatly improved understanding of the planet's internal structure and thermal evolution.

Acknowledgments

References

Anderson, J.D., Colombo, G., Esposito, P.B., Lau, E.L., Trager, G.B., 1987. The mass, gravity field and ephemeris of Mercury. Icarus 71, 337–349.

Anderson, J.D., Jurgens, R.F., Lau, E.L., Slade III, M.A., Schubert, G., 1996. Shape and orientation of Mercury from radar ranging data. Icarus 124, 690–697.

Cavanaugh, J.F., and 18 colleagues, 2007. The Mercury Laser Altimeter instrument for the MESSENGER mission. Space Sci. Rev. 131, 451–480.

Colombo, G., 1965. On the rotational period of the planet Mercury. Nature 208, 575.

Denevi, B.W., and 10 colleagues, 2009. The evolution of Mercury's crust: A newly global perspective from MESSENGER. Science 324, 613–618.

Goldreich, P., Peale, S.J., 1966. Spin orbit coupling in the Solar System. Astron. J. 71, 425–438.

Harder, H., Schubert, G., 2001. Sulfur in Mercury's core. Icarus 151, 118–122.

Harmon, J.K., Campbell, D.B., Bindschadler, D.L., Head, J.W., Shapiro, I.I., 1986. Radar altimetry of Mercury: A preliminary analysis. J. Geophys. Res. 91, 385–401.

Hauck II, S.A., Solomon, S.C., Smith, D.A., 2007. Predicted recovery of Mercury's internal structure by MESSENGER. Geophys. Res. Lett. 34, L18201. doi:10.1029/2007GL030793.

Kaula, W.M., 1966. Theory of Satellite Geodesy. Blaisdell, Waltham, Mass. 124pp.

Kaula, W.M., Schubert, G., Lingenfelter, R.E., Sjogren, W.L., Wollenhaupt, W.R., 1972. Analysis and interpretation of lunar laser altimetry. Proc. Lunar Sci. Conf. 3, 2189–2204.

Margot, J.-L., Peale, S.J., Jurgens, R.F., Slade, M.A., Holin, I.V., 2007. Large longitude libration of Mercury reveals a molten core. Science 316, 710–714.

McCarthy, J.J., Rowton, S., Moore, D., Luthcke, S., Pavlis, D.E., Tsaoussi, L.S., Rowlands, D.D., Marshall, J.A., 1994. GEODYN Systems Descriptions and Operations Manuals. NASA Goddard Space Flight Center and Hughes/STX Contractor Report, Greenbelt, Md., 358pp.

McNutt, M.K., 1984. Lithospheric flexure and thermal anomalies. J. Geophys. Res. 89, 11180–11194.

Muller, P.M., Sjogren, W.L., 1968. Mascons: Lunar mass concentrations. Science 161, 680–684.

Nimmo, F., Watters, T.R., 2004. Depth of faulting on Mercury: Implications for heat flux and effective elastic thickness. Geophys. Res. Lett. 31, L02701. doi:10.1029/2003GL018847.

Peale, S.J., 1976. Does Mercury have a molten core? Nature 262, 765–766.

Peale, S.J., Phillips, R.J., Solomon, S.C., Smith, D.E., Zuber, M.T., 2002. A procedure for determining the nature of Mercury's core. Meteorit. Planet. Sci. 37, 1269–1283.

Rowlands, D.D., Marshall, J.A., McCarthy, J.J., Rowton, S.C., Moore, D., Pavlis, D.E., Luthcke, S.B., 1993. GEODYN II System Description. Hughes-STX Contractor Report, Greenbelt, Md., 203pp.

Santo, A.G., and 25 colleagues, 2001. THE MESSENGER mission to Mercury: Spacecraft and mission design. Planet. Space Sci. 49, 1481–1500.

Schaber, G.G., Boyce, J.M., Trask, N.J., 1977. Moon–Mercury: Large impact structures, isostasy and average crustal viscosity. Phys. Earth Planet. Inter. 15, 189–201.

Smith, D.E., Sjogren, W.L., Tyler, G.L., Balmino, G., Lemoine, F.G., Konopliv, A.S., 1999. The gravity field of Mars: Results from Mars Global Surveyor. Science 286, 94–97.

Solomon, S.C., and 10 colleagues, 2008. Return to Mercury: A global perspective on MESSENGER's first Mercury flyby. Science 321, 59–62.

Spudis, P.D., Guest, J.E., 1988. Stratigraphy and geologic history of Mercury. In: Vilas, F., Chapman, C.R., Matthews, M.S. (Eds.), Mercury. University of Arizona Press, Tucson, Ariz, pp. 118–164.

Spudis, P.D., Strobell, M.E., 1984. New identification of ancient multi-ring basins on Mercury and implications for geologic evolution. Lunar Planet. Sci. 15, 814–815.

Srinivasan, D.K., Fielhauer, K.B., Smith, D.E., Zuber, M.T., 2007. The MESSENGER radio frequency tracking system. Space Sci. Rev. 131, 557–571.

Sun, X., Cavanaugh, J.F., Smith, J.C., Bartels, A.E., 2004. Design and performance measurement of the Mercury Laser Altimeter. Conference on Laser and Electro Optics (CLEO), vol. 2, pp. 16–21. doi:10.1109/CLEO.2004.1360680.

Turcotte, D.L., Willemann, R.J., Haxby, W.F., Norberry, J., 1981. Role of membrane stresses in the support of planetary topography. J. Geophys. Res. 86, 3951–3959.

Watters, T.R., Schultz, R.A., Robinson, M.S., Cooke, A.C., 2002. The mechanical and thermal structure of Mercury's early lithosphere. Geophys. Res. Lett. 29, 1542. doi:10.1029/2001GL014308.

Watters, T.R., Head, J.W., Solomon, S.C., Robinson, M.S., Chapman, C.R., Denevi, B.W., Fassett, C.I., Murchie, S.L., Strom, R.G., 2009. Evolution of the Rembrandt impact basin on Mercury. Science 324, 618–621.

Wieczorek, M.A., 2007. Gravity and topography of the terrestrial planets. In: Spohn, T. (Ed.), Treatise on Geophysics, Planets and Moons, vol. 10. Elsevier, pp. 165–206.

Zuber, M.T., and 13 colleagues, 2008. Laser altimeter observations from MESSENGER's first Mercury flyby. Science 321, 77–79.

Zuber, M.T. and 12 colleagues, 2010. Accommodation of lithospheric shortening on Mercury from altimetric profiles of ridges and lobate scarps measured during MESSENGER flybys 1 and 2. Icarus 209, 247–255.